



Assembling Co clusters via nanosized ZIF-67 sprouted from CoAl-LDH nanoflower for selective hydrogenation

Huiling Zhang^a, Xiaomei Zhou^a, Longxin Liu^a, Fujun Lan^a, Teng Zhao^a, Mo Qiu^{b,*},
Qingxin Guan^{a,*}, Wei Li^{a,*}

^a College of Chemistry, State Key Laboratory of Elemento-Organic Chemistry, Key Laboratory of Advanced Energy Materials Chemistry (Ministry of Education), Nankai University, Tianjin 300071, China

^b Agro-Environmental Protection Institute, Chinese Academy of Agricultural Sciences, No. 31, Fukang Road, Nankai District, Tianjin 300191, China

ARTICLE INFO

Keywords:

Biomass conversion
Co clusters
Multifunctional catalyst
Selective hydrogenation

ABSTRACT

Atomically dispersed cluster catalysts own versatile applications in biomass valorization, while the controllable assembly and microenvironmental regulation remain a crucial challenge. Herein, Co clusters assembled via nanosized ZIF-67 sprouted from Co-Al layered double hydroxide nanoflowers were applied for selective hydrogenation of furfural (FAL). The pyrolysis temperature can tune the microstructures and acid properties of the catalyst, which accounts for the hydrogenation of FAL to furfuryl alcohol (FOL), 2-methylfuran (2-MF), and tetrahydrofurfuryl alcohol (THFOL) with yield of 99.1 %, 96.7 %, and 82.3 %, respectively. The Co clusters favor C=O bond adsorption via bridging-type adsorption mode while suppressing the furan ring adsorption. Moreover, ultra-dispersed Co clusters facilitate the cleavage of C-OH bonds in FOL intermediate, leading to a high 2-MF yield. As the pyrolysis temperature increase, the formed Co nanoparticles are conducive to the parallel adsorption of FAL, resulting in the production of THFOL. This work affords a multi-functional catalyst in catalytic biomass upgrading.

1. Introduction

Biomass, as the only natural, renewable organic carbon resource, can be applied to produce chemicals essential for the economic and social development, which helps to conquer the energy crisis and environmental issues. [1,2]. Lignocellulose, which makes up the main structural component of plants, is by far the most abundant terrestrial biomass type and renewable resource [3,4]. The catalytic conversion of lignocellulosic biomass to liquid fuels and high-value chemicals plays a critical role in achieving carbon emissions reduction and global carbon neutrality [5]. Furfural (FAL), a vital platform molecule derived from lignocellulose, can be transformed into varieties of fuel additives and chemicals such as furfuryl alcohol (FOL), tetrahydrofurfuryl alcohol (THFOL), 2-methylfuran (2-MF), tetrahydrofuran (THF), and 2-pentanol (2-PEAL), etc (Scheme 1) [6–8]. Notably, 2-MF, a crucial chemical, is widely used in second-generation liquid fuels, gasoline additives, green solvents, perfume additives, and drug intermediates [9,10]. Hydrodeoxygenation (HDO) is regarded as the most efficient method to produce 2-MF from FAL [11]. Nevertheless, the intricate reaction pathway

of FAL hydrogenation poses a challenging obstacle to selective control over the target product (Scheme 1). As an illustration, the conversion of FAL to 2-MF involves selective hydrogenation of the carbonyl group (C=O) followed by cleavage of the hydroxyl group (C-OH) at the side of the furan ring while maintaining the integrity of the ring structure [12]. Therefore, more active metal sites and harsh reaction condition are usually indispensable to improve the selectivity of 2-MF. However, these conditions often result in the occurrence of side reactions.

In recent years, considerable efforts have been devoted to improving the conversion efficiency of FAL as well as the product selectivity of 2-MF and a series of noble metal catalysts such as Ir/C, Pt/Mg(Al)O@Al₂O₃, Ru/C, etc. with excellent catalytic performance have been developed [11–13]. However, the costly price and natural scarcity of noble metals, restrain their large-scale applications. Non-noble metal catalysts, especially Cu-based catalysts, show high activities in FAL conversion to 2-MF, of which the Cu-Cr catalyst possesses a decent catalytic performance in the industrial production of 2-MF [13,14]. Unfortunately, the environmental toxicity of Cr and the harsh reaction conditions (10–15 MPa H₂, 200–250 °C) limited its applications. Hence,

* Corresponding authors.

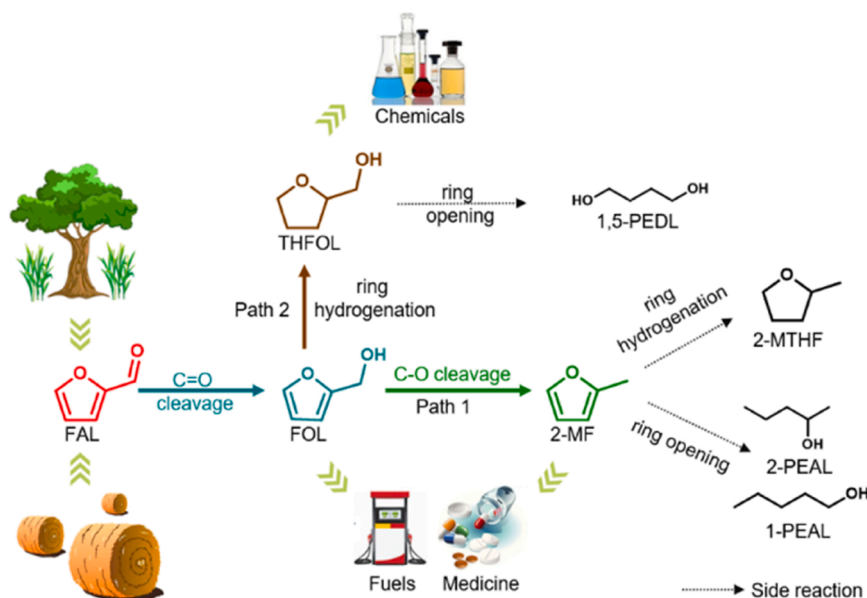
E-mail addresses: qiumo@mail.nankai.edu.cn (M. Qiu), qingxinguan@nankai.edu.cn (Q. Guan), weili@nankai.edu.cn (W. Li).

<https://doi.org/10.1016/j.apcatb.2023.123026>

Received 25 April 2023; Received in revised form 14 June 2023; Accepted 21 June 2023

Available online 22 June 2023

0926-3373/© 2023 Elsevier B.V. All rights reserved.



Scheme 1. The reaction pathways for hydrogenation/hydrogenolysis of furfural and plausible side reactions.

the development of novel Cr-free metal catalysts has drawn much attention for the catalytic synthesis of 2-MF. Recently, cobalt-based catalysts have attracted extensive attention in the selective hydrogenation of biomass-derived platform molecules due to their unique isotropic features, theoretically high catalytic activity and low cost [2,15]. Sanjay et al. fabricated a Cu-Co/Al₂O₃ catalyst by the impregnation method, which afforded a 2-MF yield of 87 % at 220 °C under 4 MPa H₂ after 5 h [16]. Lee et al. reported a ZIF-67-derived Co/NC catalyst, delivering a 100 % FAL conversion with 2-MF selectivity of 57.5 % at 180 °C under 2 MPa H₂ for 10 h [15]. However, owing to the poor ability to activate H₂ of these catalytic systems, severe reaction conditions are required to attain a comparable activity with noble metals but the uncontrollable side reactions lead to a low 2-MF selectivity. Additionally, the high temperature and high pressure conditions also cause a series of safety and energy consumption issues [17,18]. Therefore, the rational design of Co-based catalysts is essential for the conversion of FAL to 2-MF with high selectivity at mild conditions.

Atomically dispersed Co cluster catalysts with almost fully exposed active sites can significantly enhance the atom utilization efficiency, thereby showing excellent catalytic activity. Moreover, the unique Co clusters sites will engender a particular adsorption configuration of the substrate, especially the terminal adsorption, which tends to selectively produce a specific product. Fu et al. synthesized a ZrREnOx supported Co cluster catalyst by a simple impregnation method, which exhibited high catalytic activity toward FAL hydrogenation to FOL in water [19]. Saim et al. reported an intrazeolite cobalt cluster catalyst prepared via an ion-exchange process, which exhibited ultra-high turnover frequency and high catalytic activity in hydrolysis of sodium borohydride to hydrogen [20]. Although Co cluster catalysts have high catalytic activity, the stability problem caused by agglomeration and sintering in catalytic processes remains to be settled. Hence, the high interest in Co clusters focuses on the controllable preparation and stability improvement [21].

To achieve this goal, metal-embedded carbon-based catalysts derived from metal-organic frameworks (MOFs) may be promising alternatives [22–24]. Actually, the MOFs have been utilized as sacrificial templates to create carbon-based functional nanomaterials via carbonization/pyrolysis treatment, due to the ordered arrangement of organic linkers and metal ions [25–27]. However, after being pyrolyzed, the MOF crystals with a large specific surface area will collapse into a bulk phase and cause the destruction of the pore structure, which largely

hinders the mass transfer and reduces the catalytic performance [28]. Therefore, an appropriate template utilized as both the substrate and metal source for the crystallization growth of MOFs and subjected to a pyrolysis treatment could obtain metal-embedded carbon-based materials with relatively large surface area and well-dispersed active sites. This inspires us to use layered double hydroxides (LDHs) as both a substrate and a metal source, which have specific layered structures and versatile chemical compositions, enabling the cationic laminate as nucleation sites for the in-situ growth of MOFs [9,29].

In this work, we fabricated CoAl-LDHs nanoflowers precursor by regulating the molar ratio of Co/Al, and then nanosized ZIF-67 was in-situ sprouted by etching Co ions on the surface of CoAl-LDH with 2-methylimidazole ligand to form a composite ZIF-67 @CoAl-LDH. Finally, the ultrafine Co clusters embedded in carbon matrix were obtained via pyrolysis treatment while the migration of Co on LDH surface will expose a large number of Lewis acid sites. The microstructure and acid-base properties can be adjusted by varying the pyrolysis conditions, leading to interesting properties that affect the hydrogenation reaction path and selectivity. This nanocomposite can selectively upgrade furfural to produce a variety of high value-added chemicals in a single catalytic system.

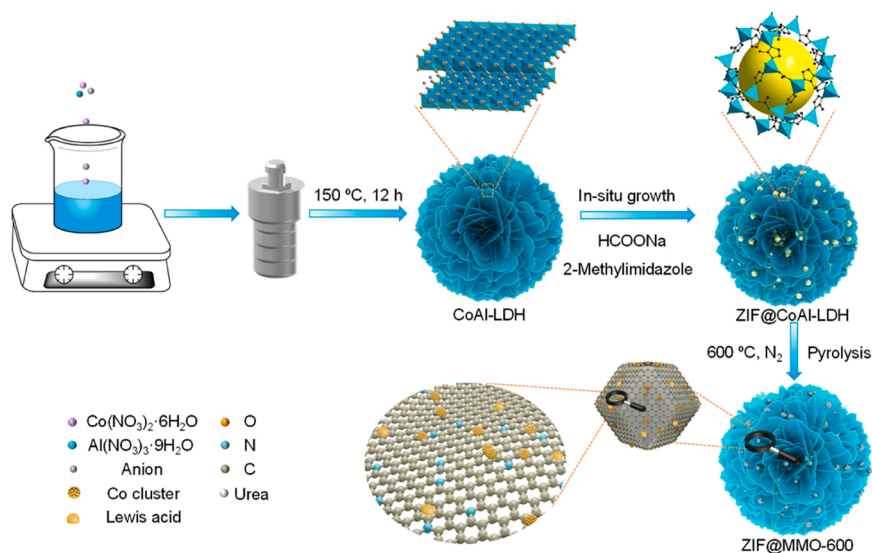
2. Experimental section

2.1. Chemicals

Analytical grade furfural (99 %), FOL (98 %), 2-MF (98 %), isopropanol (i-PrOH) (≥99.5 %), THFOL (98 %), and methanol (98 %) were purchased from Aladdin Co., Ltd. Co(NO₃)₂·6 H₂O (98 %), Al₂(NO₃)₃·9 H₂O (99 %), urea (99 %), HCOONa (99.9 %), and 2-methylimidazole were purchased from Macklin Co., Ltd.

2.2. Preparation of Co_xAl_{1-x}-LDHx and Co_xAl_{1-x}-MMO

A series of flower-like Co_xAl_{1-x}-LDHs were synthesized via a urea hydrothermal process. Typically, Co(NO₃)₂·6H₂O, Al(NO₃)₃·9H₂O, and urea with a molar ratio of 2: 1: 7 were dissolved in 60 mL methanol. The above mixture was stirred for 30 min and then transferred into a 60 mL Teflon-lined autoclave, sealed and heated at 150 °C for 12 h. A blue-purple precipitate was filtered, washed with deionized water several times until the pH value reached to neutralization. Subsequently, the



Scheme 2. Schematic of the ZIF@MMO-600 preparation.

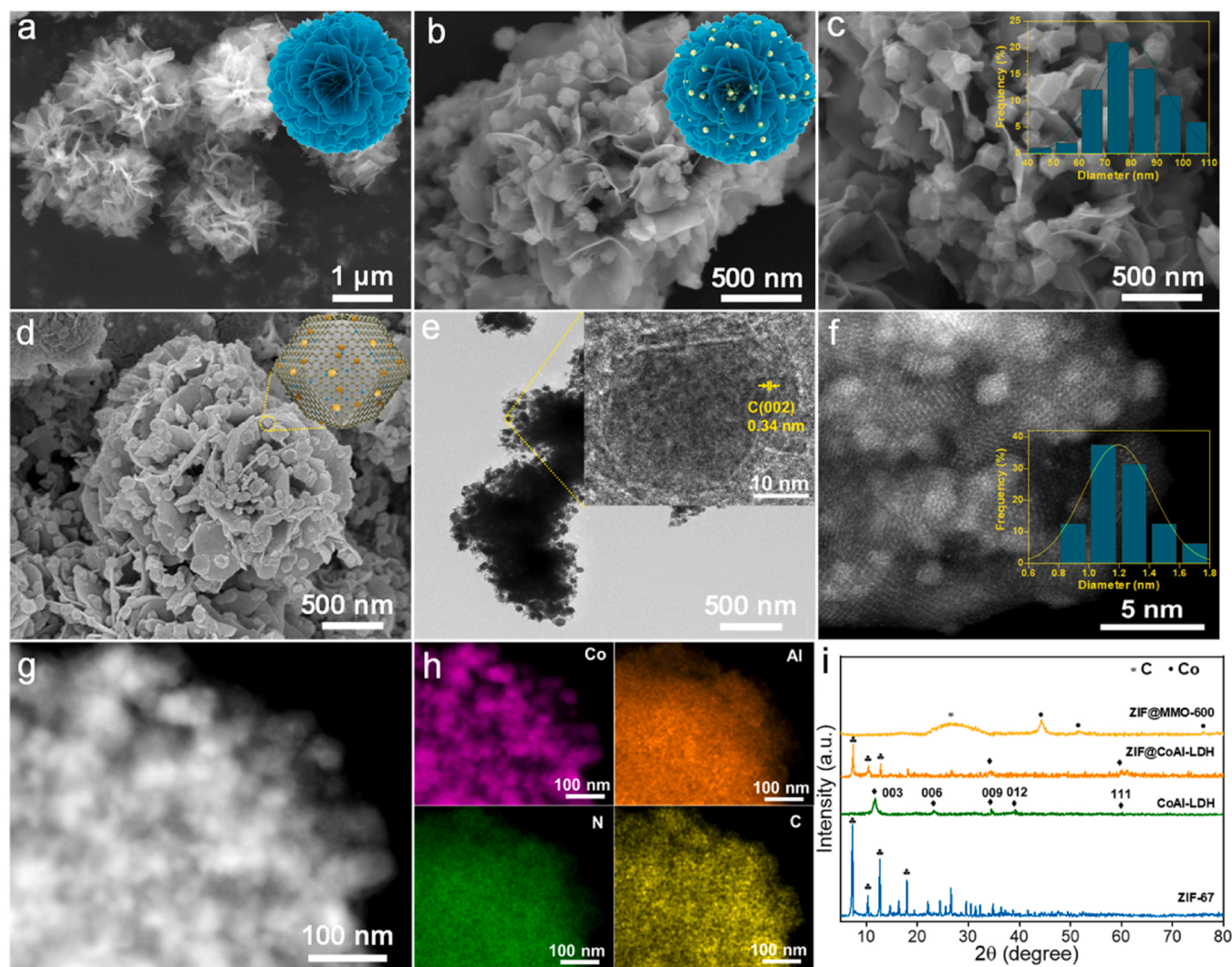


Fig. 1. SEM images of (a) $\text{Co}_2\text{Al-LDH}$, (b) $\text{ZIF@Co}_2\text{Al-LDH}$ and its large-field view (c), (d) ZIF@MMO-600 ; TEM images of the (e) ZIF@MMO-600 , and aberration corrected HAADF-STEM image of ZIF@MMO-600 (f); (g) HAADF-STEM and (h) corresponding elemental mapping images of ZIF@MMO-600 ; (i) XRD patterns of ZIF-67 , CoAl-LDH , ZIF@CoAl-LDH , and ZIF@MMO-600 .

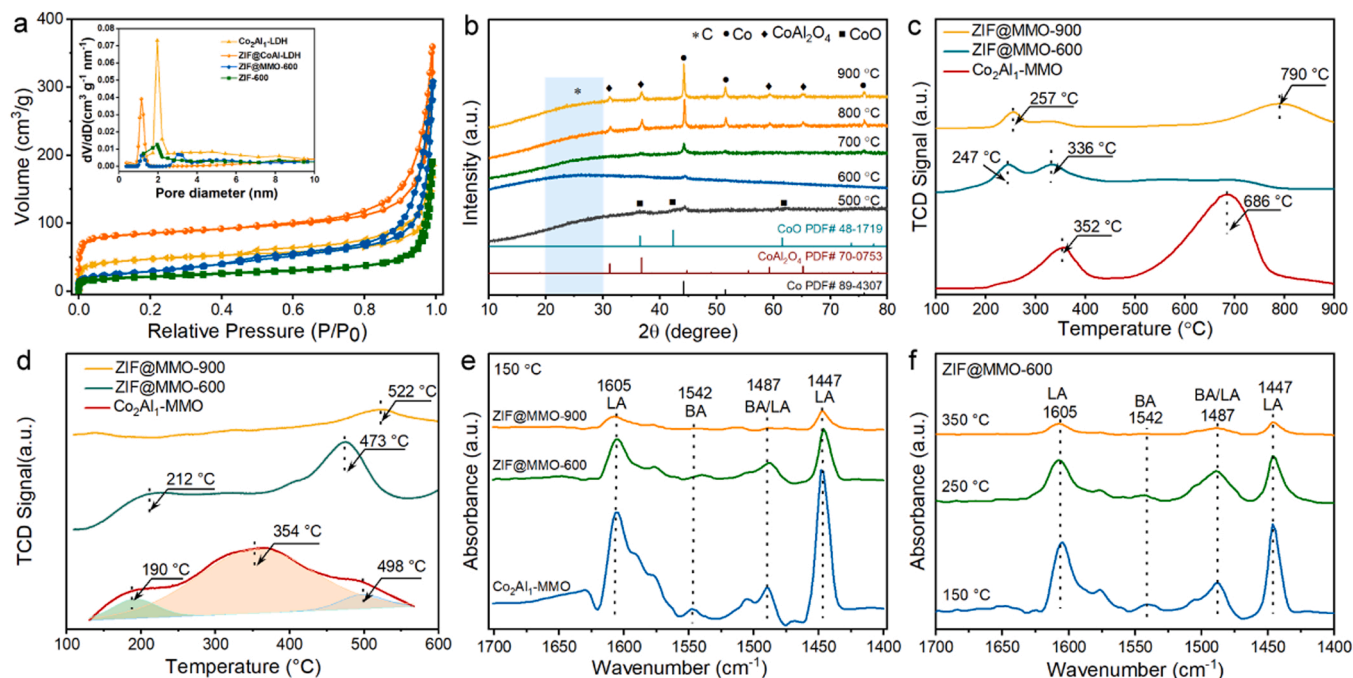


Fig. 2. (a) N_2 sorption isotherms of Co_2Al_1-LDH , $ZIF@CoAl-LDH$, $ZIF@MMO-600$, $ZIF-600$ (inset shows the pore size distribution); (b) XRD patterns of $ZIF@MMO-T$ samples; (c) H_2 -TPR profiles of Co_2Al_1-MMO , $ZIF@MMO-600$, and $ZIF@MMO-900$ samples; (d) NH_3 -TPD profiles of Co_2Al_1-MMO , $ZIF@MMO-600$, and $ZIF@MMO-900$ samples; (e) *In situ* FT-IR spectra of pyridine on various samples at 150 °C; (f) *In situ* FTIR spectra of pyridine on $ZIF@MMO-600$ at different temperature.

precipitate was dried in oven at 80 °C for 12 h, resulting in Co_2Al_1-LDH s precursors. Other Co_xAl_1-LDH s were prepared using the same method except for changing the molar ratio of Co: Al. Moreover, these Co_xAl_1-LDH s was calcined in a tube furnace at 600 °C for 4 h in nitrogen with a heating rate of 1.5 °C·min⁻¹ to obtain Co_xAl_1-MMO samples (x denotes as the molar ratio of Co: Al).

2.3. Preparation of ZIF-67 and ZIF-600

ZIF-67 were synthesized in methanol/ethanol mixed solution at room temperature. Typically, 3.94 g 2-methylimidazole were dissolved in 80 mL methanol/ethanol mixed solution with a volume ratio of 1:1, which denotes as solution A. 3.49 g $Co(NO_3)_2 \cdot 6H_2O$ were dissolved in 80 mL methanol/ethanol mixed solution, which denotes as solution B. Then solution B was poured into the solution A and stirred at room temperature for 20 h to obtain ZIF-67. The above ZIF-67 was pyrolysis in a tube furnace at 600 °C for 4 h in nitrogen with a heating rate of 1.5 °C·min⁻¹ to obtain ZIF-600 sample.

2.4. Preparation of ZIF@MMO-600 (MMO denotes as Mixed Metal Oxides)

In the typical run (Schemes 2), 1.5 g 2-methylimidazole, 0.81 g sodium formate ($HCOONa$) were dissolved in 120 mL methanol. After that, 0.72 g above Co_2Al_1-LDH was poured into the mixed solution, and stirred in 60 °C water bath for 4 h. The resultant blue-violet solid was isolated by centrifugation and then washed several times with methanol. The $ZIF@Co_2Al_1-LDH$ was obtained by drying in oven at 80 °C for 12 h and then these precursors were calcined in a tube furnace at 600 °C for 4 h in nitrogen with a heating rate of 1.5 °C·min⁻¹ to obtain $ZIF@MMO-600$ sample. Furthermore, Other $ZIF@MMO-T$ were prepared using the same method at different calcination temperature (T denotes as calcination temperature).

2.5. Catalytic evaluations

The catalytic hydrogenation of FAL were performed using a 100 mL

stainless autoclave reactor equipped with a mechanical stirring and an electric heating system. In a typical experiment, 90 mg catalyst, 2 mmol FAL, and 30 mL i-PrOH were added into autoclave reactor. The reactor was sealed and the air inside was displaced by pure H_2 for at least three times, followed by flowing pure H_2 (1–3 MPa). Then the reaction liquid was heated to the requisite temperature (180 °C) with a stirring speed of 500 rpm to trigger the hydrogenation reaction. The reaction mixture was analyzed by Agilent 7890 A gas chromatography (GC) accompanied with an HP5-MS column and the product structures were identified by gas chromatography-mass spectrometry (GCMS) using an Agilent 7890 A/5975 C spectrometer. The FAL conversion and production selectivity were calculated by the following equations:

$$\text{Conversion}(\%) = \left(1 - \frac{\text{Molar amount of FAL after reaction}}{\text{Initial molar amount of FAL fed}}\right) \times 100\% \quad (1)$$

$$\text{Selectivity}(\%) = \frac{\text{Molar amount of one product}}{\text{Total molar amount of FAL converted}} \times 100\% \quad (2)$$

2.6. Characterization

The characterizations of samples are listed in the [supporting information](#).

3. Results and discussion

A schematic of this facile, eco-friendly synthetic strategy is illustrated in Scheme 2. The $CoAl-LDH$ nanoplatelets with a well-preserved flower-like morphology were prepared by adjusting the Co/Al molar ratio from 1: 1–4: 1 (Fig. S1), the resulting Co_2Al_1-LDH possessing optimal nanoflower morphology with an average diameter of 1.5 μm (Fig. 1a). The $ZIF-67@CoAl-LDH$ composites (Fig. 1b) were fabricated by in situ sprouted of nanosized ZIF-67 on the $CoAl-LDH$ surface with sodium formate as the conditioner. A close-up scanning electron microscopy (SEM) image indicates that the dodecahedral ZIF-67 with an average diameter of 79 nm was uniformly grown on the LDH nanoplatelets (Fig. 1c), which is much smaller than the reported ZIF-67 (200–2000 nm) synthesized directly without template as a scaffold

[30,31]. Subsequently, the obtained ZIF-67 @CoAl-LDH composite was further pyrolyzed under N_2 at 600 °C for 4 h to obtain ZIF@MMO-600 sample (The other resulting samples are expressed as ZIF@MMO-T, in which T denotes as pyrolysis temperature). The SEM image in Fig. 1d showed that the ZIF@MMO-600 still maintains the well-defined 3D open-up structure after high-temperature pyrolysis treatment, which confirmed the LDH nanoplatelet afforded a stable frame for the epitaxial growth of ZIF-67 crystals. TEM image (Fig. 1e) further confirmed that the ZIF@MMO-600 maintained well-defined morphology and Co sites are surrounded by graphitic carbon layers with a crystal plane spacing of 0.34 nm (inset of Fig. 1e), which is consistent with the results of XRD (Fig. 1i). The HRTEM image and aberration corrected HAADF-STEM image of ZIF@MMO-600 reveals that highly dispersed Co clusters with a uniform size (~ 1.2 nm) are confined in the carbon matrix (Fig. 1f and Fig. S2). The elemental mapping images display the homogeneous distribution of Co, C, N and Al elements on the nanoplatelet (Figs. 1g and 1h). In contrast, a slight shrinkage and agglomeration of ZIF@MMO-900 is observed after high-temperature pyrolysis accompanied by the partial collapse of initial ZIF-67 (Fig. S3a). Correspondingly, Co clusters grow into large Co nanoparticles with apparent Co (111) lattice fringe (Fig. S3b and S3c), implying the generation of another hydrogenation active site. To give a more detailed comparative study, the Co_2Al_1 -LDH is directly reduced under 600 °C in H_2 atmosphere, and another relatively dispersed Co species anchored on mixed metal oxide laminates emerged with an average particle size of 15 nm (Fig. S4). The above cobalt sites play a decisive role in reaction path and hydrogenation selectivity.

XRD patterns of CoAl-LDH, ZIF-67, ZIF@CoAl-LDH, and its pyrolytic ZIF@MMO-600 are shown in Fig. 1i. The CoAl-LDH exhibits characteristic reflections at 11.6°, 23.3°, 34.6°, 39.1°, and 60.5°, which are assigned to (003), (006), (009), (012), and (111) plane of LDH phase, confirming the successful synthesis of LDHs [29]. Furthermore, the XRD patterns of ZIF@CoAl-LDH show the coexistence of LDH and ZIF-67 phase, indicating the successful combination of CoAl-LDH and ZIF-67 forming a novel composite material [32]. After pyrolysis under N_2 at 600 °C, the initial peaks disappeared accompanied by the appearance of new diffraction peaks at 2θ values of 26°, 44°, and 51° was observed, corresponding to the (002) plane of graphitic carbon and the (111) and (200) crystal planes of face-centered cubic Co, respectively [33]. It proves that ZIF framework transformed to graphitic carbon microstructure while the carbon reduced the adjacent $Co^{\delta+}$ to Co^0 sites via high-temperature pyrolysis, which is consistent with the HRTEM results (Figs. 1e and 1f).

The nitrogen adsorption-desorption isotherms and pore size distribution of samples are shown in Fig. 2a. It revealed that all the samples possess type-IV isotherm and H3-type hysteresis loops [34,35]. Among them, the hysteresis loop of Co_2Al_1 -LDH merely appeared in relatively higher pressure ($P/P_0 > 0.4$), demonstrating the presence of mesopores structure. In contrast, the isotherm of ZIF@CoAl-LDH exhibits sharp uptakes at relatively low pressures ($P/P_0 < 0.05$) and has a large hysteresis loop from 0.4 to 1.0, which indicates the coexistence of mesoporous and microporous structures. Moreover, the micro-/mesoporous structure still maintains in ZIF@MMO-600 sample after high-temperature pyrolysis, while the ZIF-600 sample appears much limited mesoporous. The specific surface area of ZIF@MMO-600 is $169\text{ m}^2\cdot\text{g}^{-1}$ much larger than that of ZIF-600 ($61\text{ m}^2\cdot\text{g}^{-1}$) and Co_2Al_1 -MMO ($95\text{ m}^2\cdot\text{g}^{-1}$) shown in Table S1. The results above further demonstrated that the LDH laminates as a scaffold effectively decrease the collapse of the ZIF pore structure during the pyrolysis process.

In order to research the structural evolution during pyrolysis, the ZIF@CoAl-LDH composites pyrolyzed at different temperatures were elaborately explored. As shown in Fig. S5, the TGA curve of ZIF@CoAl-LDH sample displays a slight weight loss (11.3 %) at ≈ 198 °C, which is attributed to the removal of water in the hydrotalcite layers. As the temperature increase, an abrupt weight loss (20.0 %) mainly caused by the decomposition of anions between hydrotalcite layers in the

temperature range of 198–460 °C. Above 460 °C, a continuous weight loss is observed, which is ascribed to the decomposition and carbonization of ZIF-67 accompanied by the reduction of cobalt species and the generation of graphitized carbon [36]. The Raman spectra (Fig. S6) certified the generation of graphite carbon, and the XRD patterns of pyrolyzed ZIF@MMO-500 sample also indicated that the carbon matrix begin to reduce adjacent cobalt species after pyrolysis at 500 °C (Fig. 2b). However, CoO phase (PDF# 48–1719) can still be observed in ZIF@MMO-500 sample, indicating the incomplete reduction of $Co^{\delta+}$ in the ZIF framework. Moreover, the ZIF@MMO-600 exhibits diffuse broad peaks at $2\theta = 44.2^\circ$ and 51.5° , corresponding to the (111) and (200) reflection of Co phase (PDF# 89–4307), indicating the existence of ultrafine Co clusters [37,38]. As the pyrolysis temperature increase, the diffraction peaks of Co phase become much stronger, together with the occurrence of $CoAl_2O_4$ (PDF# 70–0853), demonstrating the particle size of metal cobalt gradually increases while the metal oxides in the hydrotalcite matrix transform to spinel structure.

To further investigate the microstructures evolution of Co species during the pyrolysis process, H_2 -TPR tests were performed and displayed in Fig. 2c. It has been reported that different Co species exhibits various reduction peaks. As shown in Fig. 2c, the Co_2Al_1 -MMO sample has two reduction peaks at 352 °C and 686 °C. The peak at 352 °C is attributed to the reduction of the cobalt oxide on MMO support or the Co species with weak interactions with the MMO support, while the peak appeared at 686 °C is ascribed to the reduction of the $CoAl_2O_4$ phase in support [39]. In contrast, the ZIF@MMO-600 only shows two minor low-temperature reduction peaks at 247 and 336 °C, the reduction peak at 336 °C is also derived from the remaining cobalt oxide on the MMO support, the peak at 247 °C is the reduction of cobalt oxide formed by the inevitable oxidation of Co clusters in the carbon matrix. Similarly, a small peak at 257 °C is observed in ZIF@MMO-900 sample owing to the reduction of cobalt oxide formed by the inevitable oxidation of Co nanoparticles after contact with air. To prove it, the ZIF@LDH precursor was carried out in-situ pyrolysis in a chemical adsorption instrument followed by H_2 -TPR tests. As shown in Fig. S7, both reduction peaks at 247 °C of ZIF@MMO-600-In situ and 257 °C of ZIF@MMO-900-In situ have disappeared, which directly proved that the reduction peaks at 247 °C and 257 °C are assigned to the reduction of cobalt oxide formed by the inevitable oxidation after contact with air. Notably, the reduction peak of $CoAl_2O_4$ was not observed in ZIF@MMO-600 sample, indicating fewer spinel structures formed in this sample. In addition, the peak at 336 °C decreased in ZIF@MMO-900 sample compared with ZIF@MMO-600, while a high temperature reduction peak at 790 °C arose, indicating cobalt oxide and aluminum oxide in the support gradually transformed to $CoAl_2O_4$ after high-temperature pyrolysis. The results obtained from the above H_2 -TPR are well consistent with the XRD results.

To obtain the quantitative surface acidic sites of the catalysts, NH_3 -TPD was carried out. The corresponding acid strength and concentration of samples are listed in Table S2. As shown in Fig. 2d, the Co_2Al_1 -MMO sample exhibits three broad desorption peaks at 190, 354, and 498 °C, which are assigned to weak, medium and strong acid sites, respectively [40,41]. In comparison, the ZIF@MMO-600 sample only displays two peaks at 212 °C and 473 °C, which are attributed to weak and strong acid sites, respectively. Notably, the concentration of acid sites decreases markedly from ZIF@MMO-600 to ZIF@MMO-900, which indicates the alumina and cobalt oxide in the support gradually transform to the spinel structure with the increase of pyrolysis temperature. This transformation leads to the decrease of the surface acidic sites. The nature and amounts of surface acidic sites were identified by Py-IR analysis. Fig. 2e exhibits the Py-IR spectra of Co_2Al_1 -MMO, ZIF@MMO-600, and ZIF@MMO-900 samples toward pyridine adsorption at 40 °C after desorption at 150 °C. It can be seen that all the samples mainly show three bands: bands at 1447 cm^{-1} and 1605 cm^{-1} are assigned to the pyridine adsorbed at Lewis acidic sites; the band at 1542 cm^{-1} is generally attributed to the Brønsted acid site, while the band at

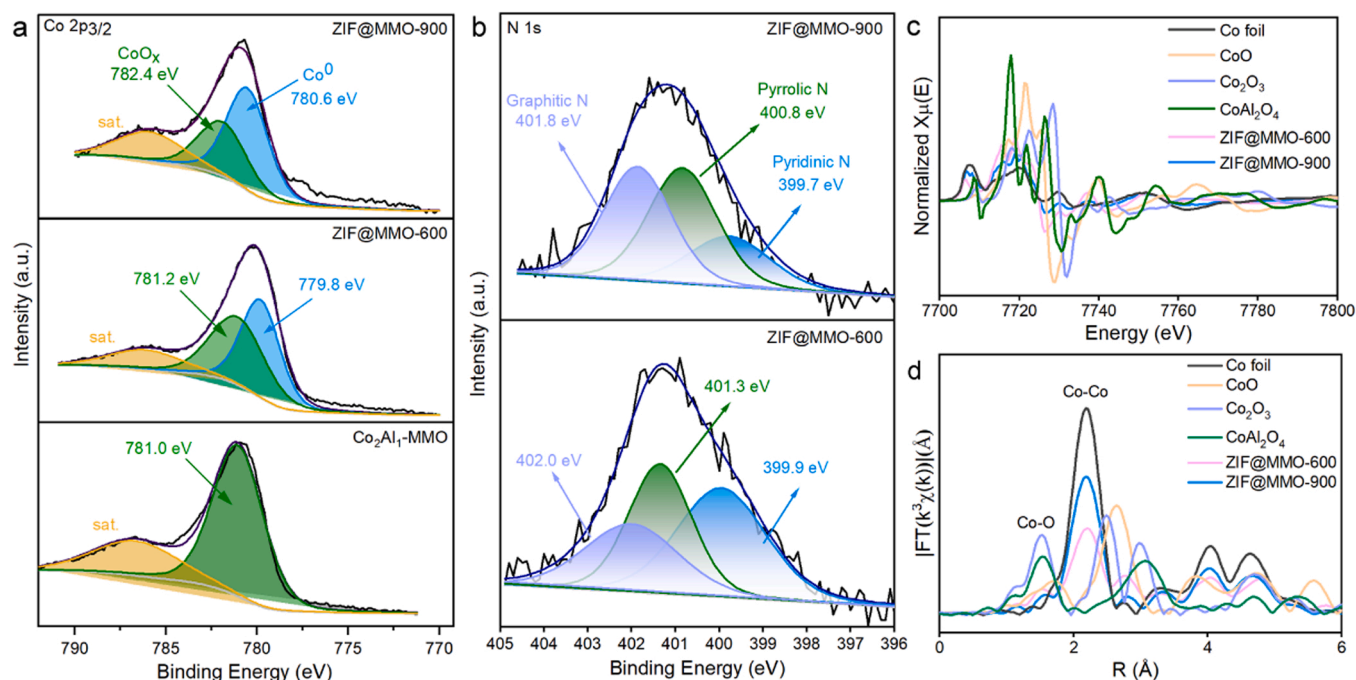


Fig. 3. XPS spectra of Co 2p_{3/2} (a) for Co₂Al₁-MMO, ZIF@MMO-600, ZIF@MMO-900 and N 1s spectra (b) for ZIF@MMO-600, ZIF@MMO-900; Normalized XANES spectra (c) and Fourier-transform EXAFS spectra (d) at Co K-edge for ZIF@MMO-600 and ZIF@MMO-900 samples.

1487 cm⁻¹ exhibits a mixture of Lewis acidic site and Brønsted acidic under pyridine adsorption [42]. It indicates that all the samples display primarily Lewis acid sites with only a small proportion of Brønsted acid sites. Furthermore, the density of both Lewis acid and Brønsted acid sites decreased with the increase of pyrolysis temperature (Table S2). It has been reported that the Lewis acid sites are mainly derived from the unsaturated Al³⁺ of CoAl-MMO [43,44], and the coordination of Al³⁺ is studied by Al XPS spectra (Fig. S8). The first peak at 74.2 eV is assigned to octahedrally coordinated Al³⁺ (Al^{VI}), whereas the second one at 73.6 eV, must be assigned to tetrahedrally coordinated Al³⁺ (Al^{IV}) [45], and the atomic ratios of them are listed in Table S3. Hence, the formation of CoAl₂O₄ leads to the reduction of Lewis acid sites. As shown in Fig. 2f, the Lewis acid sites could still be detected in the ZIF@MMO-600 catalyst after elevating the temperature to 350 °C, indicating that the strong acid sites are dominant in ZIF@MMO-600 according well with the NH₃-TPD results (Fig. 2d).

XPS was performed to explore the surface elemental compositions and chemical states of cobalt species (Figs. 3a and 3b). The high-resolution Co 2p_{3/2} spectra of Co₂Al₁-MMO show the characteristics peak of cobalt oxide species CoO_x (781.0 eV) accompany by the broad satellite peak (785.8 eV). The ZIF@MMO-600 shows two types of Co species which are attributed to Co⁰ (779.8 eV) and CoO_x (781.2 eV) [25]. Furthermore, the ZIF@MMO-900 exhibits similar situations while the binding energies of Co⁰ and CoO_x are higher than those in ZIF@MMO-600, indicating a stronger interaction between cobalt sites and support after high-temperature pyrolysis. The high-resolution N 1s spectra shows that ZIF@MMO-900 have three peaks corresponding to pyridinic N (399.7 eV), pyrrolic N (400.8 eV), and graphitic N (401.8 eV), respectively (Fig. 3b) [46]. It is noteworthy that the content of pyridinic N species reduces persistently, while the graphitic-N species increases gradually. In addition, the binding energies of N species in ZIF@MMO-900 sample are lower than that in ZIF@MMO-600, while the binding energies of Co species in ZIF@MMO-900 shift positively to higher binding energies in comparison to those of ZIF@MMO-600 sample. This movement implies that the partial electron migration from Co sites to high electronegative N sites, demonstrating that the potent electronic interaction between Co sites and N species in carbon

matrix [47].

The synchrotron XANES and the corresponding Fourier-transform EXAFS were conducted to explore the composition and structure information of the ZIF@CoAl-LDH-derived samples. As shown in Fig. 3c, the ZIF@MMO-600 and ZIF@MMO-900 display a white line intensity between CoO and Co foil, the edge feature for metal Co is found, indicating the coexistence of both a CoO_x phase and metallic Co phase. Furthermore, the white line intensity of ZIF@MMO-600 is higher than that of ZIF@MMO-900, implying that there is more metallic Co in ZIF@MMO-900. By comparison, the Co clusters in ZIF@MMO-600 are more easily oxidized due to the ultra-small particle size, in accordance with the XRD results. The EXAFS results of Co species show that metallic Co⁰ phase (2.49 Å) is dominant in those samples (50 % for ZIF@MMO-600 % and 75 % for ZIF@MMO-900, respectively) (Fig. 3d). Compared to ZIF@MMO-900, the ZIF@MMO-600 show reduced strength of the first nearest-neighbor distance, indicating the former has a lower Co-Co coordination number. The ZIF@MMO-600 shows a Co-Co coordination number of 3.6 (± 0.2), which is much lower than that of ZIF@MMO-900 sample 7.1 (± 0.2) (Table S4) [9,48]. This result indicates that there is a higher Co-Co coordination unsaturation for ZIF@MMO-600 sample, owing to its tiny Co cluster species shown in HAADF-STEM image (Fig. 1f). To further explore the surface microstructure of Co species, these two Co-based samples after acid treatment are performed XANES and the corresponding Fourier-transform EXAFS analysis by using Co foil, CoO, Co₂O₃, and CoAl₂O₄ as referencing samples (Fig. S9). The absence of Co-Co coordination at 2.49 Å in ZIF@MMO-600 and ZIF@MMO-900 samples indicated that metallic Co has been completely removed by pickling. Moreover, the ZIF@MMO-600 sample presents obvious edge features of Co₂O₃, while the edge feature of CoAl₂O₄ is dominant in ZIF@MMO-900 sample, indicating that most of the metal oxides on the LDH laminate are transformed into spinel structure after high-temperature pyrolysis, consisting with the XRD results. Similarly, the Co Fourier-transform EXAFS spectrum further reveals that the Co-O coordination in ZIF@MMO-600 mainly derived from CoO and the Co-O coordination in ZIF@MMO-900 mainly derived from CoAl₂O₄ phase (Fig. S9b). Furthermore, no obvious Co-N_x coordination appears, indicating that the main active sites come from Co-Co coordination.

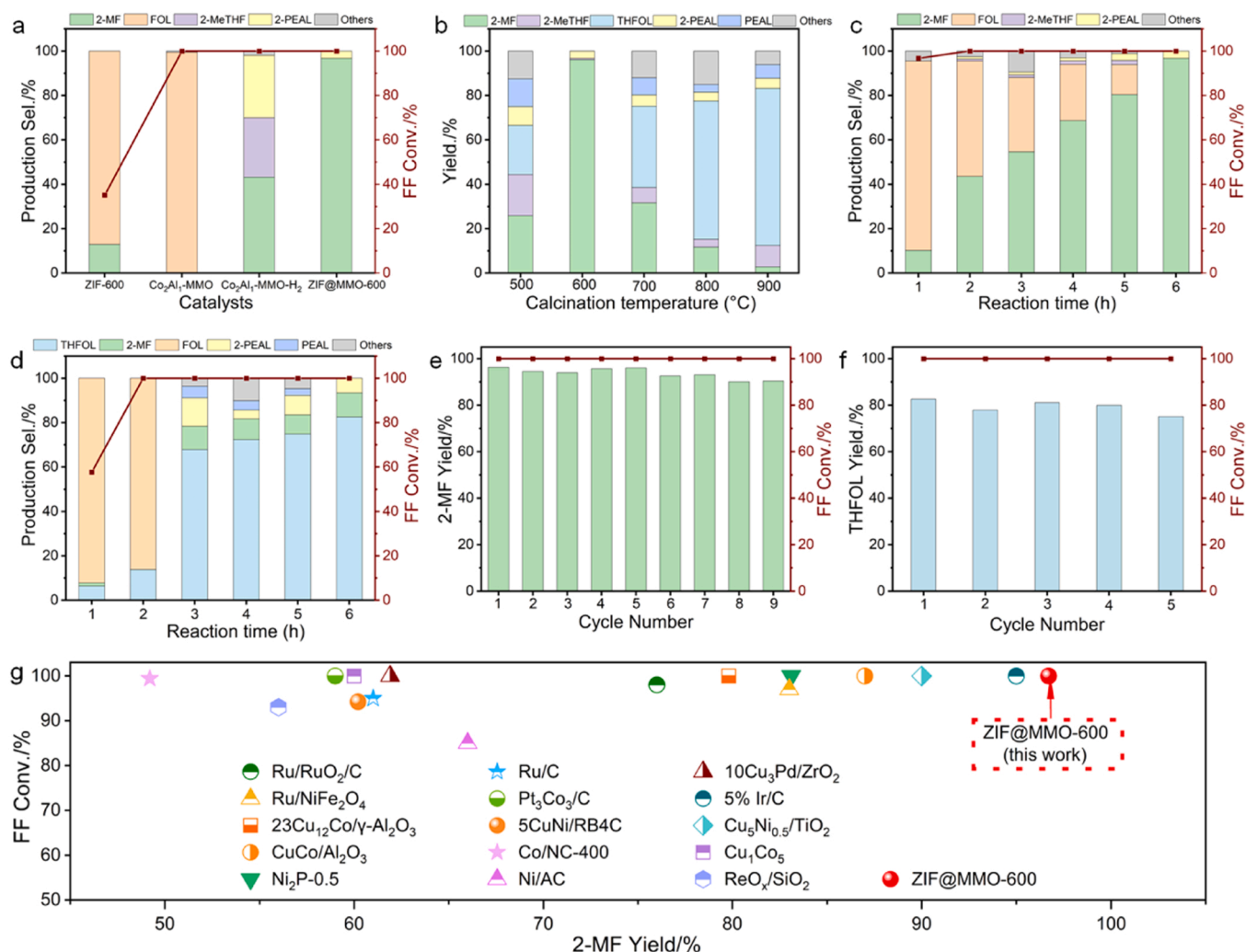


Fig. 4. (a) Catalytic performance for selective hydrogenation of FAL over different cobalt-based catalysts; (b) Effect of pyrolysis temperature on the conversion and selectivity over ZIF@LDH-T samples. Catalytic selective hydrogenation of FAL as a function of reaction time by ZIF@LDH-600 (c) and ZIF@LDH-900 (d). Stability of catalysts: ZIF@MMO-600 (e) and ZIF@MMO-900 (f). (g) The FAL conversion and 2-MF yield of ZIF@MMO-600 compared with those of most state-of-the-art catalysts (references [7–21] of Supporting Information and Table S5). Reaction condition: 2 mmol FAL, 90 mg catalyst, 30 mL i-PrOH, 180 °C, 1 MPa H₂ (a, b, c, e), 3 MPa H₂ (d, f).

3.1. Catalytic performance of ZIF@LDHs-derived catalysts

The catalytic performance of the prepared cobalt-based catalysts was explored toward selective hydrogenation of FAL under relatively mild conditions. As shown in Fig. 4a, the equivalent ZIF-600 exhibits 35.1 % FAL conversion and 87.1 % FOL selectivity after 6 h at 180 °C, accompanied by the production of 2-MF (12.9 %). Co₂Al₁-MMO shows high carbonyl (C=O) hydrogenation activity with ~100 % FAL conversion and 99 % FOL selectivity, correspondingly, which also has the highest surface Lewis acid density measured by Py-IR analysis (Fig. 2e). In view of this result, it can speculate that Lewis acid sites play a crucial role in activating the C=O bond, thereby driving the conversion of FAL to FOL [42]. After reduced under H₂ flow at 600 °C, the obtained Co₂Al₁-MMO-H₂ sample shows ~100 % FAL conversion, while the selectivity toward the target product (2-MF) is relatively low (43.2 %), together with unavoidable furan ring (C=C) hydrogenation. Dramatically, the ZIF@CoAl-LDH-derived ZIF@MMO-600 sample shows the optimal catalytic performance with a 2-MF yield of 96.7 %, which is attributed to the synergistic effect of Lewis acid sites and highly dispersed cobalt clusters certified by Py-IR spectrum (Fig. 2e) and HAADF-STEM image (Fig. 1f). As far as we know, this catalytic behavior is comparable to most noble metal catalysts and distinguished non-noble metallic

catalysts (Fig. 4g and Table S5).

To explore the effect of pyrolysis conditions on the structure and properties of as-prepared catalysts, ZIF@CoAl-LDH-derived samples pyrolyzed at different temperatures were evaluated in selective hydrogenation of FAL. As shown in Fig. 4b, all the ZIF@MMO-T (T denotes as pyrolysis temperature) samples exhibit complete FAL conversion after 6 h under 1 MPa H₂ pressure, while the product distribution is diverse. The ZIF@MMO-500 shows poor product selectivity, owing to the complex active sites and incomplete reduction of Co³⁺ in the ZIF framework. Notably, the ZIF@MMO-600 exhibits the optimal 2-MF yield of 96.7 %, indicating an almost complete inhibition of C=C hydrogenation and concurrently strong hydrogenolysis of C-OH bond. Further elevating the pyrolysis temperature, the products of C=C bond hydrogenation increase gradually. When the pyrolysis temperature rises to 900 °C, the yield of THFOL reached 70.7 % after 6 h at 1 MPa H₂ pressure. It demonstrated that the large cobalt particles confined in the carbon matrix are more conducive to hydrogenation of the furan ring. Fig. S10 shows the catalytic performance of ZIF@MMO-600 and ZIF@MMO-900 catalysts at diverse temperature and H₂ pressure, from which the ZIF@MMO-600 sample shows a slightly drop in 2-MF yield from 96.7 % to 90.9 % with the boost the H₂ pressure from 1 MPa to 3 MPa, indicating excessive pressure will cause hydrogenation of furan ring even

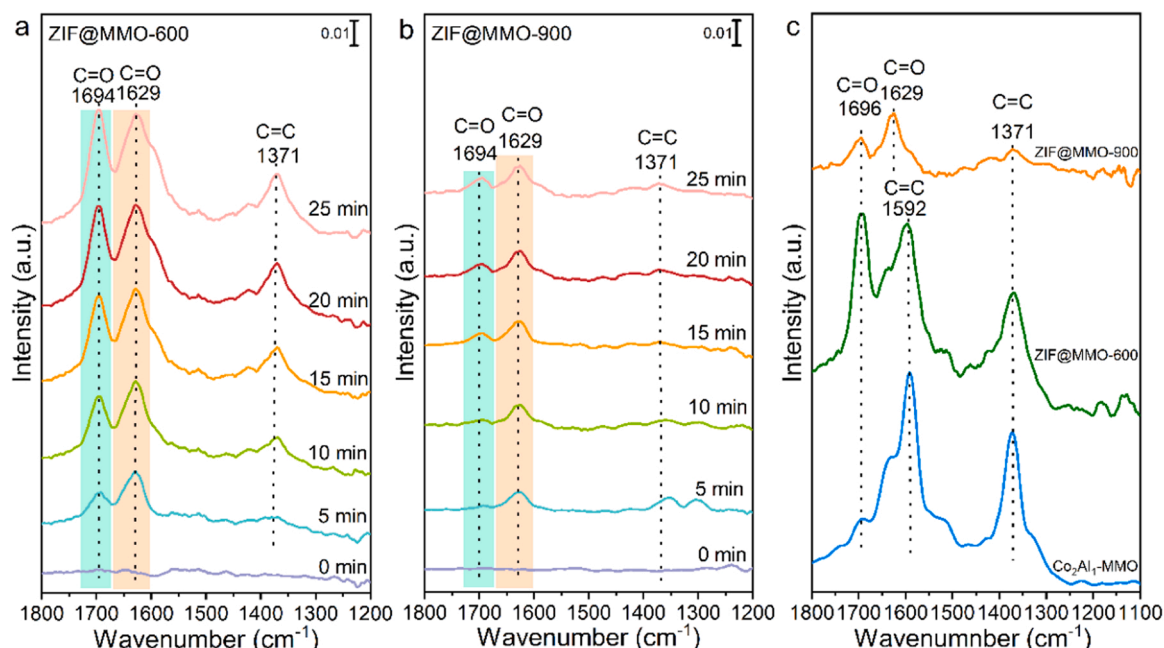


Fig. 5. *In situ* FT-IR spectra of adsorbed FAL on ZIF@MMO-600 (a) and ZIF@MMO-900 (b); (c) *In situ* FT-IR spectra of FAL adsorption on Co₂Al₁-MMO, ZIF@MMO-600 and ZIF@MMO-900, recorded after flowing FAL for 30 min at 80 °C and subsequent argon flushing for 30 min.

ring opening of furan ring. In addition, the high reaction temperature is conducive to the production of 2-MF, and the optimal parameters for ZIF@MMO-600 is 1 MPa of H₂ and 180 °C reaction temperature in 6 h. For the ZIF@MMO-900 catalyst, the increasing H₂ pressure and reaction temperature can improve the selectivity of THFOL, and the current optimal yield was 82.3 % at 3 MPa H₂ and 180 °C after 6 h.

For ZIF@MMO-600 (Fig. 4c), the FAL conversion of 96.8 % was achieved at the beginning of the reaction (1 h), together with the production of 85.3 % FOL and a small amount of 2-MF (10.2 %). The selectivity of 2-MF increased gradually from 10.2 % to 96.7 % after 6 h, while the selectivity of FOL exhibited an opposite tendency. The above results demonstrate that strong hydrogenolysis of C-OH group occurs on the surface of ZIF@MMO-600 sample while suppressing the furan ring hydrogenation. In contrast, the ZIF@MMO-900 shows lower hydrogenation activity, with only 57.7 % conversion of FAL after 1 h at 3 MPa H₂ pressure (Fig. 4d) together with FOL being the main product (92.3 %) and a little 2-MF (1.3 %). As the reaction proceeds, the selectivity of FOL decreased gradually and even disappeared completely after 3 h, accompanied by the formation of THFOL (Yield: 82.3 %). It indicates that the hydrogenation of furan ring occurs on the surface of ZIF@MMO-900, and the FAL molecules undergo parallel adsorption on Co nanoparticles (NPs) sites.

The stability of ZIF@MMO-600 and ZIF@MMO-900 samples under optimal reaction conditions was tested. As shown in Fig. 4e, the conversion of FAL was still ~100 % and the yield of 2-MF exceeded 90 % after 9 time recycles, implying having strong interactions between Co clusters and carbon matrix derived from ZIF@CoAl-LDH. In addition, the ZIF@MMO-900 sample can be used for 5 cycles without obvious decrease of activity and selectivity under harsh reaction conditions (180 °C, 3 MPa H₂, 6 h), indicating satisfactory stability (Fig. 4f). The XRD patterns of fresh and used catalysts indicate that the crystal structure and particle size of Co have no obvious change before and after use (Fig. S11a). The Co loading of ZIF@MMO-600 sample only declined from 48.7 % to 47.1 % within 5 cycles (0.32 % per run) while the Co loading of ZIF@MMO-900 sample dropped from 45.8 % to 41.1 % after 5 cycles (0.94 % per run), implying that without distinct loss occurred during this high-temperature liquid phase reaction (Table S6). The nitrogen adsorption-desorption isotherms of ZIF@MMO-600 and ZIF@MMO-900 catalysts indicate that the surface area and pore volume

of above samples only dropped a little before and after use (Fig. S11b). Furthermore, those catalysts have a strong magnetism and can be separated quickly in 10 s from liquid, which is conducive to the recycling of catalysts. These results demonstrate that ZIF@LDH-derived ZIF@MMO-600 and ZIF@MMO-900 catalysts display desirable stability in FAL conversion, probably attributed to the confinement effect between the carbon matrix and Co sites.

To study the adsorption mode of substrate on the surface of catalysts, *in situ* FT-IR spectra were applied on the ZIF@LDH-derived catalysts. Generally, the pure gas phase FAL shows strong peaks at 1703, 1562, and 1473 cm⁻¹, which are attributed to ν (C=O), furan ring breath, and ν (C=C) on the furan ring, respectively [49,50]. As shown in Fig. 5a, the ZIF@MMO-600 emerged two strong adsorptions of C=O at 1694 cm⁻¹ and 1629 cm⁻¹ at the beginning of the exposure (5 min), and the intensity of peaks have no obvious change with the extension of exposure time. Meanwhile, a red-shift of ν (C=O) was observed from 1703 cm⁻¹ to 1694 cm⁻¹ accompanied by a shoulder peak at 1634 cm⁻¹ appears, indicating C=O adsorption undergoes η^2 (C, O) configuration at the outset [51,52]. The peak at 1371 cm⁻¹ is attributed to ν (C=C) breath. It is reported that the chemical adsorption of the furan ring in the sample will lead to the disappearance of the C=C bond and the furan ring breath [9,51]. The obvious peak at 1371 cm⁻¹ can be observed in ZIF@MMO-600 sample, demonstrating no chemical adsorption of furan ring. In contrast, the ZIF@MMO-900 sample shows two ν (C=O) breath and obvious ν (C=C) band at 1353 cm⁻¹ for short contact with FAL (5 min), implying strong adsorption of C=O band via main η^2 (C, O) configuration and physical adsorption of the furan ring (Fig. 5b). With the extension of exposure time, the intensity of ν (C=C) progressively decreased while the ν (C=O) become stronger, implying the planar adsorption of furan ring on ZIF@MMO-900 catalyst surface [53].

When the saturated samples were purged under argon gas flow, the peaks of gas phase and physical adsorption were weakened, and the chemical adsorption was well maintained (Fig. 5c) [12,54]. For Co₂Al₁-MMO, the two ν (C=C) breath in furan ring at 1592 and 1371 cm⁻¹ can be observed, accompanied by a weak ν (C=O) breath at 1696 cm⁻¹, indicating the furfural molecules underwent rather weak chemical adsorption of C=O band and physical adsorption of the furan ring on the surface of Co₂Al₁-MMO. The ZIF@MMO-600 sample showed strong ν (C=O) and ν (C=C), indicating only C=O underwent activation

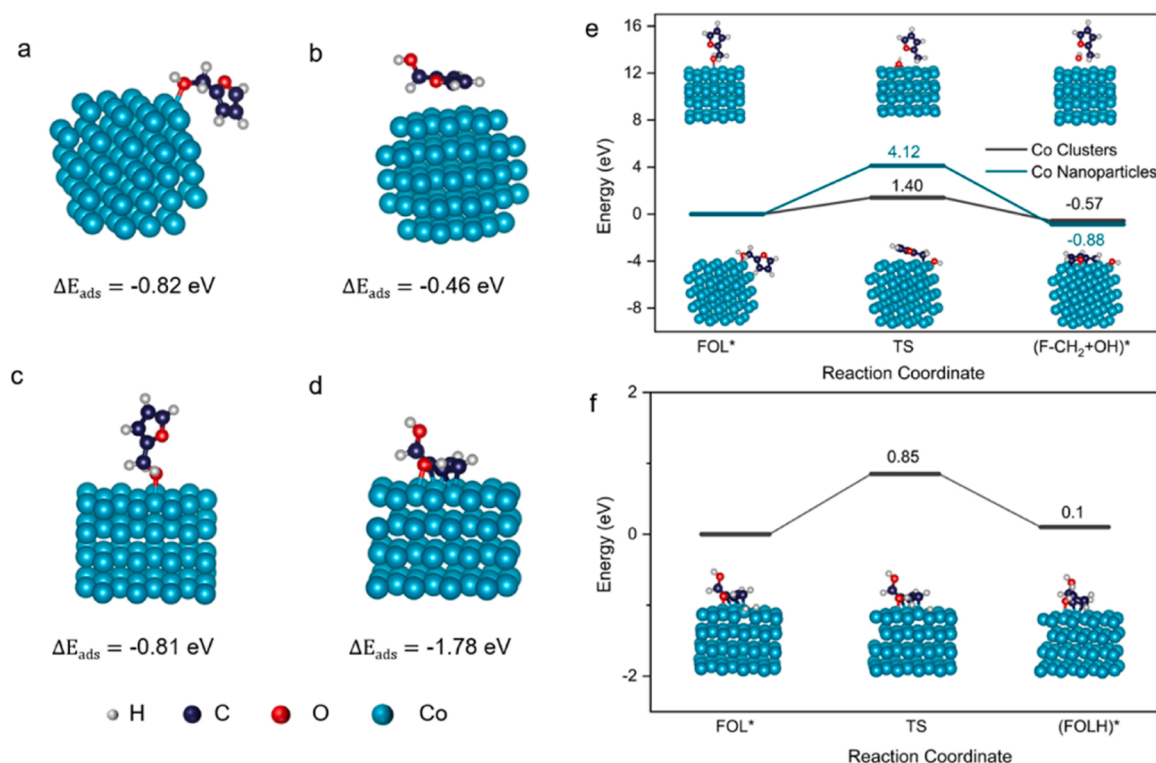
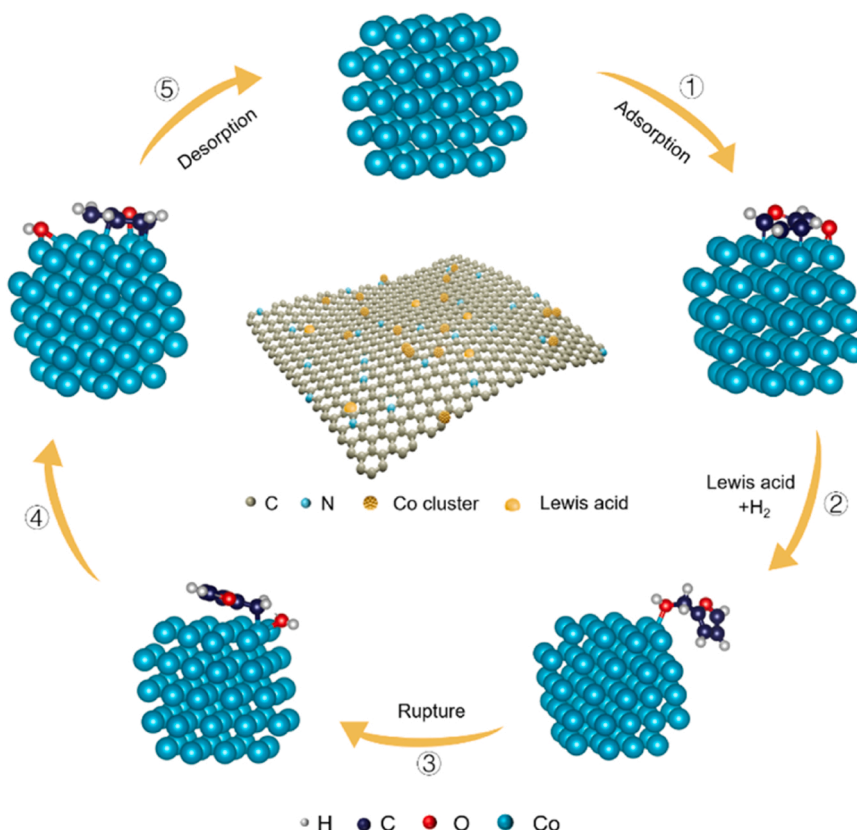


Fig. 6. DFT optimized adsorption modes and adsorption energies of FOL on Co clusters (a, b) and Co (111) slabs (c, d); Energies profiles and corresponding optimized structures for: (e) C-OH band rupture in FOL (Path1), (f) C=C band (furan ring) hydrogenation in FOL (Path 2) on the surface of Co clusters (black line) and Co (111) nanoparticles (cyan line), respectively.

adsorption and the adsorption of furan ring is markedly inhibited. In contrast, in the case of ZIF@MMO-900 sample, the intensity of $\nu(\text{C}=\text{O})$ is relatively weak and the $\nu(\text{C}=\text{C})$ band is negligible, demonstrating both C=O bond and furan ring underwent chemisorption on the surface of ZIF@MMO-900 sample. As expected, in the case of ZIF@MMO-600, FAL molecules undergo activation adsorption of C=O band with bridge adsorption on Co clusters, facilitating the cleavage of C-OH band and the formation of 2-MF. As for ZIF@MMO-900 sample, FAL molecules undergo chemisorption of both C=O band and furan ring with parallel adsorption on the surface of CoNPs, resulting the full hydrogenation of C=O band and furan ring to produce THFOL. The adsorption mode of FAL molecules plays a key role in the hydrogenation reaction path and product selectivity, which will be further discussed in the following density functional theory (DFT) calculation.

DFT calculation was conducted to explore the substrate adsorption modes, reaction pathway, and product selectivity on ZIF@MMO-600 and ZIF@MMO-900 samples. Metallic Co slabs with (111) plane and Co clusters (1.0 nm) (Fig. S12) were selected as two representative calculation modes based on the results of XRD and HRTEM. Above all, the adsorption configuration of FAL molecule was taken as the research object. As for the ZIF@MMO-600 sample, the optimal adsorption state (Fig. S13a and S13b) of FAL is C=O band bridge adsorption on the Co clusters via Co-O₂ band and Co-C₅ band, with the band length of 1.968 Å and 2.037 Å, and the furan ring undergoes physical adsorption on the surface of Co clusters via Co-C₂ and Co-C₄ band. This unique adsorption configuration of FAL on the surface of ZIF@MMO-600 effectively promotes the activation and rupture of C=O band and inhibits the activation of furan ring. The adsorption energy (E_{ad}) of above terminal adsorption mode is -2.16 eV. In contrast, on the ZIF@MMO-900 sample, the optimal adsorption mode (Fig. S13c and S13d) of FAL is that both C=O band and furan ring parallel adsorbed on the hollow sites of Co (111) slabs with lower adsorption energy of -1.97 eV, in which both the furan ring and C=O are effectively activated. The above results are in keeping with the *In situ* FT-IR measurements (Fig. 5).

As the most important intermediate, the conversion path of FOL directly determines the selectivity of furfural hydrogenation products. The optimal adsorption mode of FOL is determined by comparing the adsorption energy of various adsorption modes. All the adsorption configurations and their adsorption energies of FOL are listed in Fig. S14, in the presence of ZIF@MMO-600, the C-OH group of FOL undergoes the terminal adsorption on Co clusters with the lowest adsorption energies of -0.82 eV and the band length of C-OH is prominently extended to 1.481 Å (Fig. 6a), indicating that the Co clusters sites significantly enhanced the ability to activate and rupture the C-OH bond. In the case of ZIF@MMO-900 sample, the optimal FOL adsorption is that the furan ring undergoes parallel adsorption on the surface of Co (111) slabs with the lowest adsorption energy of -1.78 eV (Fig. 6d), in which the furan ring is effectively activated. According to the adsorption modes investigative above, the potential hydrogenation reaction paths of FOL on the surface of Co clusters and Co (111) nanoparticles were explored in detail. Its corresponding energy barriers for C-OH bond rupture and C=C bond (furan ring) hydrogenation are shown in Figs. 6e and 6f. In the progress of C-OH bond rupture (Path 1), FOL is firstly adsorbed to the surface of Co clusters and Co (111) nanoparticles, followed by C-OH bond activation and rupture to form methylene furan and hydroxyl species. The energy barriers of this reaction path over Co cluster and Co (111) nanoparticle are 1.40 eV and 4.12 eV, respectively, demonstrating the unique terminal adsorption mode C-OH in FOL is thermodynamically advantageous on the surface of Co Clusters (Fig. 6e). In addition, the C=C band (furan ring) hydrogenation in FOL progress, the energy barrier in Co (111) nanoparticle is merely 0.85 eV, much lower than C-OH bond rupture (4.12 eV), indicating C=C band hydrogenation is rather easy on surface of Co (111) nanoparticle. Significantly, in the process of theoretical simulation, we found that the hydrogenation of C=C bond in the furan ring is almost impossible for FOL molecule on the surface of Co clusters, which may be related to the truth that it is difficult for the furan ring undergoing parallel adsorption on the surface of Co clusters.



Scheme 3. Schematic illustration for the reaction mechanism of furfural hydrogenation to 2-MF on the surface of ZIF@MMO-600.

Based on the results of DFT calculation and *In situ* FT-IR above, the reaction mechanism of FAL hydrogenation to 2-MF over ZIF@MMO-600 is clarified in Scheme 3. The ultrafine Co cluster site is conducive to the bridge adsorption of C=O bond in furfural, which promoted the activation and rupture of C=O while inhibiting the adsorption of furan ring, resulting the enhancement in the selectivity of 2-MF. The catalytic hydrogenation process of FAL to 2-MF over ZIF@MMO-600 is shown as follows: (1) FAL molecule undergoes adsorption and activation over ZIF@MMO-600 via C=O band bridge adsorption on the surface of Co clusters; (2) The active H atom attacks the C atom and O atom in the carbonyl group with the assistance of Lewis acids to form a terminal adsorbed FOL molecule; (3) FOL intermediate experiences C-OH band rupture to produce methylene furan and hydroxyl species. (4) Methylene furan and hydroxyl combine with active H to produce 2-MF and water. (5) The resulting 2-MF desorbs from the ZIF@MMO-600 surface.

4. Conclusion

In this work, we have successfully fabricated a novel ultrafine Co cluster catalyst with well-designed morphology and highly dispersed active sites via nanosized ZIF-67 sprouted from CoAl-LDH nanoflower followed by pyrolysis treatment. Notably, the pyrolysis temperature can be used to modify the microstructures and acid properties of the catalyst, leading to selective hydrogenation of FAL to produce FOL, 2-MF, and THFOL with the yield of 99.1 %, 96.7 %, and 82.3 %, respectively. Characterizations and DFT calculation results prove that Lewis acid sites facilitate the activation of C=O band and highly dispersed Co cluster sites is conducive to the bridge adsorption of C=O of FAL via Co-C and Co-O band, whilst the adsorption of furan ring is effectively inhibited. Moreover, the Co cluster sites promote the activation and cleavage of C-OH in FOL with the lowest energy barrier, thereby boosting the selectivity of 2-MF. In contrast, the parallel adsorption is predominant on the surface of Co NPs, which contributes to the activation adsorption of both

the C=O group and C=C band in the furan ring, resulting in the production of THFOL. This work provides a novel strategy to precisely control hydrogenation selectivity by tuning microstructure and acid properties of ZIF@LDH-derived nanocomposites. Moreover, a delicate combination of LDHs and MOFs affords a promising application for energy storage and conversion.

CRediT authorship contribution statement

Huiling Zhang: Conceptualization, Methodology, Software, Data curation, Writing – original draft. **Xiaomei Zhou:** Software, Investigation, Formal analysis. **Longxin Liu:** Methodology, Investigation. **Fujun Lan:** Software, Formal analysis. **Teng Zhao:** Investigation. **Mo Qiu:** Conceptualization, Writing – review & editing. **Qingxin Guan:** Conceptualization, Visualization, Writing – review & editing. **Wei Li:** Conceptualization, Methodology, Resources, Supervision, Funding acquisition.

Declaration of Competing Interest

The authors declare no conflict of interest.

Data Availability

Data will be made available on request.

Acknowledgments

We acknowledge the financial support from the National Natural Science Foundation of China (NSFC, 22172082 and 21978137), NCC Fund (NCC2020FH05), and the Fundamental Research Funds for the Central Universities.

Appendix A. Supporting information

Supplementary data associated with this article can be found in the online version at [doi:10.1016/j.apcatb.2023.123026](https://doi.org/10.1016/j.apcatb.2023.123026).

References

- [1] F. Lan, H. Zhang, C. Zhao, Y. Shu, Q. Guan, W. Li, Copper clusters encapsulated in carbonaceous mesoporous silica nanospheres for the valorization of biomass-derived molecules, *Acs. Catal.* 12 (2022) 5711–5725, <https://doi.org/10.1021/acscatal.2c01270>.
- [2] S. Xiang, L. Dong, Z.-Q. Wang, X. Han, L.L. Daemen, J. Li, Y. Cheng, Y. Guo, X. Liu, Y. Hu, A.J. Ramirez-Cuesta, S. Yang, X.-Q. Gong, Y. Wang, A unique Co@CoO catalyst for hydrogenolysis of biomass-derived 5-hydroxymethylfurfural to 2,5-dimethylfuran, *Nat. Commun.* 13 (2022) 3657, <https://doi.org/10.1038/s41467-022-31362-9>.
- [3] M. Liu, B. Han, P.J. Dyson, Simultaneous generation of methyl esters and CO in lignin transformation, *Angew. Chem. Int. Ed.* 61 (2022), e202209093, <https://doi.org/10.1002/anie.202209093>.
- [4] W. Deng, Y. Feng, J. Fu, H. Guo, Y. Guo, B. Han, Z. Jiang, L. Kong, C. Li, H. Liu, P.T. Nguyen, P. Ren, F. Wang, S. Wang, Y. Wang, Y. Wang, S.S. Wong, K. Yan, N. Yan, X. Yang, Y. Zhang, Z. Zhang, X. Zeng, H. Zhou, Catalytic conversion of lignocellulosic biomass into chemicals and fuels, *Green. Energy Environ.* 8 (2023) 10–114, <https://doi.org/10.1016/j.gee.2022.07.003>.
- [5] Y. Liu, G. Li, Y. Hu, A. Wang, F. Lu, J.-J. Zou, Y. Cong, N. Li, T. Zhang, Integrated conversion of cellulose to high-density aviation fuel, *Joule* 3 (2019) 1028–1036, <https://doi.org/10.1016/j.joule.2019.02.005>.
- [6] W. Liu, Y. Yang, L. Chen, E. Xu, J. Xu, S. Hong, X. Zhang, M. Wei, Atomically-ordered active sites in NiMo intermetallic compound toward low-pressure hydrodeoxygenation of furfural, *Appl. Catal. B-Environ.* 282 (2021), 119569, <https://doi.org/10.1016/j.apcatb.2021.119569>.
- [7] S. Tian, W. Gong, W. Chen, N. Lin, Y. Zhu, Q. Feng, Q. Xu, Q. Fu, C. Chen, J. Luo, W. Yan, H. Zhao, D. Wang, Y. Li, Regulating the catalytic performance of single-atomic-site ir catalyst for biomass conversion by metal-support interactions, *Acs. Catal.* 9 (2019) 5223–5230, <https://doi.org/10.1021/acscatal.9b00322>.
- [8] C. Wang, L. Wang, J. Zhang, H. Wang, J.P. Lewis, F.-S. Xiao, Product selectivity controlled by zeolite crystals in biomass hydrogenation over a palladium catalyst, *J. Am. Chem. Soc.* 138 (2016) 7880–7883, <https://doi.org/10.1021/jacs.6b04951>.
- [9] X. Meng, L. Wang, L. Chen, M. Xu, N. Liu, J. Zhang, Y. Yang, M. Wei, Charge-separated metal-couple-site in NiZn alloy catalysts towards furfural hydrodeoxygenation reaction, *J. Catal.* 392 (2020) 69–79, <https://doi.org/10.1016/j.jcat.2020.10.003>.
- [10] Y. Deng, R. Gao, L. Lin, T. Liu, X.-D. Wen, S. Wang, D. Ma, Solvent tunes the selectivity of hydrogenation reaction over α -MoC catalyst, *J. Am. Chem. Soc.* 140 (2018) 14481–14489, <https://doi.org/10.1021/jacs.8b09310>.
- [11] P. Sudarsanam, E. Peeters, E.V. Makshina, V.I. Parvulescu, B.F. Sels, Advances in porous and nanoscale catalysts for viable biomass conversion, *Chem. Soc. Rev.* 48 (2019) 2366–2421, <https://doi.org/10.1039/C8CS00452H>.
- [12] S. Chen, R. Wojcieszak, F. Dumeignil, E. Marceau, S. Royer, How catalysts and experimental conditions determine the selective hydroconversion of furfural and 5-hydroxymethylfurfural, *Chem. Rev.* 118 (2018) 11023–11117, <https://doi.org/10.1021/acs.chemrev.8b00134>.
- [13] H.-Y. Zheng, J. Yang, Y.-L. Zhu, G.-W. Zhao, Synthesis of γ -butyrolactone and 2-methylfuran through the coupling of dehydrogenation and hydrogenation over copper-chromite catalyst, *React. Kinet. Catal. L.* 82 (2004) 263–269, <https://doi.org/10.1023/B:REAC.0000034836.56895.a9>.
- [14] B. Li, L. Li, H. Sun, C. Zhao, Selective deoxygenation of aqueous furfural to 2-methylfuran over Cu⁰/Cu₂O-SiO₂ sites via a copper phyllosilicate precursor without extraneous gas, *ACS Sustain. Chem. Eng.* 6 (2018) 12096–12103, <https://doi.org/10.1021/acssuschemeng.8b02425>.
- [15] J.G. Lee, S. Yoon, E. Yang, J.H. Lee, K. Song, H.R. Moon, K. An, Structural evolution of ZIF-67-derived catalysts for furfural hydrogenation, *J. Catal.* 392 (2020) 302–312, <https://doi.org/10.1016/j.jcat.2020.10.014>.
- [16] S. Srivastava, G.C. Jadeja, J. Parikh, Copper-cobalt catalyzed liquid phase hydrogenation of furfural to 2-methylfuran: An optimization, kinetics and reaction mechanism study, *Chem. Eng. Res. Des.* 132 (2018) 313–324, <https://doi.org/10.1016/j.cherd.2018.01.031>.
- [17] S.K. Jaatinen, R.S. Karinen, J.S. Lehtonen, Liquid phase furfural hydrotreatment to 2-methylfuran with carbon supported copper, nickel, and iron catalysts, *ChemistrySelect* 2 (2017) 51–60, <https://doi.org/10.1002/slct.201601947>.
- [18] G. Giorgianni, S. Abate, G. Centi, S. Perathoner, S. van Beuzekom, S.-H. Soo-Tang, J.C. Van der Waal, Effect of the solvent in enhancing the selectivity to furan derivatives in the catalytic hydrogenation of furfural, *ACS Sustain. Chem. Eng.* 6 (2018) 16235–16247, <https://doi.org/10.1021/acssuschemeng.8b03101>.
- [19] Y. Ma, G. Xu, H. Wang, Y. Wang, Y. Zhang, Y. Fu, Cobalt nanocluster supported on zrenox for the selective hydrogenation of biomass derived aromatic aldehydes and ketones in water, *Acs. Catal.* 8 (2018) 1268–1277, <https://doi.org/10.1021/acscatal.7b03470>.
- [20] M. Rakap, S. Özkaz, Intrazeolite cobalt (0) nanoclusters as low-cost and reusable catalyst for hydrogen generation from the hydrolysis of sodium borohydride, *Appl. Catal. B-Environ.* 91 (2009) 21–29, <https://doi.org/10.1016/j.apcatb.2009.05.014>.
- [21] S. Özkaz, R.G. Finke, Nanocluster formation and stabilization fundamental studies: ranking commonly employed anionic stabilizers via the development, then application, of five comparative criteria, *J. Am. Chem. Soc.* 124 (2002) 5796–5810, <https://doi.org/10.1021/ja012749v>.
- [22] S. Yuan, Z. Pu, H. Zhou, J. Yu, I.S. Amiin, J. Zhu, Q. Liang, J. Yang, D. He, Z. Hu, G. Van Tendeloo, S. Mu, A universal synthesis strategy for single atom dispersed cobalt/metal clusters heterostructure boosting hydrogen evolution catalysis at all pH values, *Nano Energy* 59 (2019) 472–480, <https://doi.org/10.1016/j.nanoen.2019.02.062>.
- [23] H. Li, M. Zhang, W. Zhou, J. Duan, W. Jin, Ultrathin 2d catalysts with n-coordinated single Co atom outside Co cluster for highly efficient Zn-air battery, *Chem. Eng. J.* 421 (2021), 129719, <https://doi.org/10.1016/j.cej.2021.129719>.
- [24] Y. Xiong, J. Dong, Z.-Q. Huang, P. Xin, W. Chen, Y. Wang, Z. Li, Z. Jin, W. Xing, Z. Zhuang, J. Ye, X. Wei, R. Cao, L. Gu, S. Sun, L. Zhuang, X. Chen, H. Yang, C. Chen, Q. Peng, C.-R. Chang, D. Wang, Y. Li, Single-atom Rh/N-doped carbon electrocatalyst for formic acid oxidation, *Nat. Nanotechnol.* 15 (2020) 390–397, <https://doi.org/10.1038/s41565-020-0665-x>.
- [25] W. Gong, Y. Lin, C. Chen, M. Al-Mamun, H.-S. Lu, G. Wang, H. Zhang, H. Zhao, Nitrogen-doped carbon nanotube confined Co-Nx sites for selective hydrogenation of biomass-derived compounds, *Adv. Mater.* 31 (2019), 1808341, <https://doi.org/10.1002/adma.201808341>.
- [26] L. Zhu, X.-Q. Liu, H.-L. Jiang, L.-B. Sun, Metal-organic frameworks for heterogeneous basic catalysis, *Chem. Rev.* 117 (2017) 8129–8176, <https://doi.org/10.1021/acs.chemrev.7b00091>.
- [27] J. Sun, L. Tao, C. Ye, Y. Wang, G. Meng, H. Lei, S. Zheng, C. Xing, X. Tao, P. Wu, J. Chen, S. Du, D. Wang, Y. Li, MOF-derived Ru₁Zr₁/Co dual-atomic-site catalyst with promoted performance for fischer-tropsch synthesis, *J. Am. Chem. Soc.* <https://doi.org/10.1021/jacs.2c09168>.
- [28] M. Luo, M. Li, B. Lü, Q. Liu, Z. Di, L. Guo, Cobalt nanoparticle-decorated LDH/ZIF-derived porous nanoplatelets for fischer-tropsch synthesis, *ACS Appl. Nano Mater.* 4 (2021) 3734–3741, <https://doi.org/10.1021/acsnanm.1c00177>.
- [29] H. Zhang, J. Dong, X. Qiao, J. Qin, H. Sun, A. Wang, L. Niu, G. Bai, In-situ generated highly dispersed nickel nanoclusters confined in mgal mixed metal oxide platelets for benzoic acid hydrogenation, *J. Catal.* 372 (2019) 258–265, <https://doi.org/10.1016/j.jcat.2019.03.012>.
- [30] H.-C. Li, W.-J. Liu, H.-X. Han, H.-Q. Yu, Hydrophilic swellable metal-organic framework encapsulated pd nanoparticles as an efficient catalyst for Cr(VI) Reduct., *J. Mater. Chem. A* 4 (2016) 11680–11687, <https://doi.org/10.1039/C6TA03688K>.
- [31] D. Saliba, M. Ammar, M. Rammal, M. Al-Ghoul, M. Hmadeh, Crystal growth of ZIF-8, ZIF-67, and their mixed-metal derivatives, *J. Am. Chem. Soc.* 140 (2018) 1812–1823, <https://doi.org/10.1021/jacs.7b11589>.
- [32] M. Shao, F. Ning, Y. Zhao, J. Zhao, M. Wei, D.G. Evans, X. Duan, Core-shell layered double hydroxide microspheres with tunable interior architecture for supercapacitors, *Chem. Mater.* 24 (2012) 1192–1197, <https://doi.org/10.1021/cm203831p>.
- [33] J. Tang, R.R. Salunkhe, J. Liu, N.L. Torad, M. Imura, S. Furukawa, Y. Yamauchi, Thermal conversion of core-shell metal-organic frameworks: a new method for selectively functionalized nanoporous hybrid carbon, *J. Am. Chem. Soc.* 137 (2015) 1572–1580, <https://doi.org/10.1021/ja511539a>.
- [34] H. Zhong, J. Wang, Y. Zhang, W. Xu, W. Xing, D. Xu, X. Zhang, ZIF-8 derived graphene-based nitrogen-doped porous carbon sheets as highly efficient and durable oxygen reduction electrocatalysts, *Angew. Chem., Int. Ed.* 126 (2014) 14459, <https://doi.org/10.1002/ange.201408990>.
- [35] X. Qiao, T. She, H. Zhang, X. Wen, L. Niu, L. Ricardez-Sandoval, J. Li, G. Bai, One-pot synthesis of porous silica-supported ultrafine ni nanoparticles as efficient and stable catalyst for selective hydrogenation of benzophenone, *Appl. Catal. B-Environ.* 259 (2019), 118111, <https://doi.org/10.1016/j.apcatb.2019.118111>.
- [36] Z. Li, M. Shao, L. Zhou, R. Zhang, C. Zhang, M. Wei, D.G. Evans, X. Duan, Directed growth of metal-organic frameworks and their derived carbon-based network for efficient electrocatalytic oxygen reduction, *Adv. Mater.* 28 (2016) 2337–2344, <https://doi.org/10.1002/adma.201505086>.
- [37] X. Li, C. Zeng, J. Jiang, L. Ai, Magnetic cobalt nanoparticles embedded in hierarchically porous nitrogen-doped carbon frameworks for highly efficient and well-recyclable catalysis, *J. Mater. Chem. A* 4 (2016) 7476–7482, <https://doi.org/10.1039/C6TA01054G>.
- [38] J. Wang, R. Nie, L. Xu, X. Lyu, X. Lu, Catalytic transfer hydrogenation of oleic acid to octadecanol over magnetic recoverable cobalt catalysts, *Green. Chem.* 21 (2019) 314–320, <https://doi.org/10.1039/C8GC03075H>.
- [39] Z. Xia, L. Niu, Y. An, G. Bian, T. Li, G. Bai, Ni-Al/CoOx-catalyzed hydrodeoxygenation of 5-hydroxymethylfurfural into 2,5-dimethylfuran at low temperatures without external hydrogen, *Green. Chem.* 23 (2021) 7763–7772, <https://doi.org/10.1039/D1GC02758A>.
- [40] H. Zhang, J. Dong, Y. Li, F. Chen, R. Zhang, X. Xiang, R. Liu, J. He, S. Zhang, Synthesis of tunable-acidity vanadium phosphorus oxide catalysts modified by layered double oxide for the selective oxidation of n-butane, *Ind. Eng. Chem. Res.* 61 (2022) 3850–3859, <https://doi.org/10.1021/acs.iecr.1c03760>.
- [41] R.J. Chimentão, B.C. Miranda, D. Ruiz, F. Gispert-Guirado, F. Medina, J. Llorca, J. B.O. Santos, Catalytic performance of zinc-supported copper and nickel catalysts in the glycerol hydrogenolysis, *J. Energy Chem.* 42 (2020) 185–194, <https://doi.org/10.1016/j.jechem.2019.07.003>.
- [42] H. Zhang, W. Yang, I.I. Roslan, S. Jaenicke, G.-K. Chuah, A combo Zr-HY and Al-HY zeolite catalysts for the one-pot cascade transformation of biomass-derived furfural to γ -valerolactone, *J. Catal.* 375 (2019) 56–67, <https://doi.org/10.1016/j.jcat.2019.05.020>.
- [43] V.K. Díez, J.I. Di Cosimo, C.R. Apesteguía, Study of the citral/acetone reaction on mgalox oxides: Effect of the chemical composition on catalyst activity, selectivity

- and stability, *Appl. Catal. A-Gen.* 345 (2008) 143–151, <https://doi.org/10.1016/j.apcata.2008.04.035>.
- [44] G. Cui, X. Meng, X. Zhang, W. Wang, S. Xu, Y. Ye, K. Tang, W. Wang, J. Zhu, M. Wei, D.G. Evans, X. Duan, Low-temperature hydrogenation of dimethyl oxalate to ethylene glycol via ternary synergistic catalysis of Cu and acid-base sites, *Appl. Catal. B-Environ.* 248 (2019) 394–404, <https://doi.org/10.1016/j.apcatb.2019.02.042>.
- [45] J.S. Valente, E. Lima, J.A. Toledo-Antonio, M.A. Cortes-Jacome, L. Lartundo-Rojas, R. Montiel, J. Prince, Comprehending the thermal decomposition and reconstruction process of sol-gel MgAl layered double hydroxides, *J. Phys. Chem. C* 114 (2010) 2089–2099, <https://doi.org/10.1021/jp910538r>.
- [46] Y. He, S. Hwang, D.A. Cullen, M.A. Uddin, L. Langhorst, B. Li, S. Karakalos, A. J. Kropf, E.C. Wegener, J. Sokolowski, M. Chen, D. Myers, D. Su, K.L. More, G. Wang, S. Litster, G. Wu, Highly active atomically dispersed CoN₄ fuel cell cathode catalysts derived from surfactant-assisted MOFs: carbon-shell confinement strategy, *Energ. Environ. Sci.* 12 (2019) 250–260, <https://doi.org/10.1039/C8EE02694G>.
- [47] X. Han, W. Zhang, X. Ma, C. Zhong, N. Zhao, W. Hu, Y. Deng, Identifying the activation of bimetallic sites in NiCo₂S₄@g-C₃N₄-CNT hybrid electrocatalysts for synergistic oxygen reduction and evolution, *Adv. Mater.* 31 (2019), 1808281, <https://doi.org/10.1002/adma.201808281>.
- [48] W. Gong, Q. Yuan, C. Chen, Y. Lv, Y. Lin, C. Liang, G. Wang, H. Zhang, H. Zhao, Liberating n-cnts confined highly dispersed Co-N_x sites for selective hydrogenation of quinolines, *Adv. Mater.* 31 (2019), 1906051, <https://doi.org/10.1002/adma.201906051>.
- [49] H. Daly, H.G. Manyar, R. Morgan, J.M. Thompson, J.J. Delgado, R. Burch, C. Hardacre, Use of short time-on-stream attenuated total internal reflection infrared spectroscopy to probe changes in adsorption geometry for determination of selectivity in the hydrogenation of citral, *ACS Catal.* 4 (2014) 2470–2478, <https://doi.org/10.1021/cs500185n>.
- [50] Q. Wang, J. Feng, L. Zheng, B. Wang, R. Bi, Y. He, H. Liu, D. Li, Interfacial structure-determined reaction pathway and selectivity for 5-(hydroxymethyl) furfural hydrogenation over Cu-based catalysts, *ACS Catal.* 10 (2020) 1353–1365, <https://doi.org/10.1021/acscatal.9b03630>.
- [51] W. Yu, K. Xiong, N. Ji, M.D. Porosoff, J.G. Chen, Theoretical and experimental studies of the adsorption geometry and reaction pathways of furfural over FeNi bimetallic model surfaces and supported catalysts, *J. Catal.* 317 (2014) 253–262, <https://doi.org/10.1016/j.jcat.2014.06.025>.
- [52] S.H. Krishna, L. Zhang, I. Hermans, G.W. Huber, T.F. Kuech, J.A. Dumesic, Rates of levoglucosanol hydrogenolysis over Brønsted and Lewis acid sites on platinum silica-alumina catalysts synthesized by atomic layer deposition, *J. Catal.* 389 (2020) 111–120, <https://doi.org/10.1016/j.jcat.2020.05.025>.
- [53] X. Meng, Y. Yang, L. Chen, M. Xu, X. Zhang, M. Wei, A control over hydrogenation selectivity of furfural via tuning exposed facet of Ni catalysts, *ACS Catal.* 9 (2019) 4226–4235, <https://doi.org/10.1021/acscatal.9b00238>.
- [54] F. Delbecq, P. Sautet, Competitive C=C and C=O adsorption of α - β -unsaturated aldehydes on Pt and Pd surfaces in relation with the selectivity of hydrogenation reactions: a theoretical approach, *J. Catal.* 152 (1995) 217–236, <https://doi.org/10.1006/jcat.1995.1077>.